Proceedings of the Canadian Society for Mechanical Engineering International Congress
32nd Annual Conference of the Computational Fluid Dynamics Society of Canada
Canadian Society of Rheology Symposium
CSME/CFDSC/CSR 2025
May 25–28, 2025, Montréal, Québec, Canada

NUMBER

Computational Investigation of Strain-Vorticity Interactions in Wingtip Vortex Formation

Guang C. Deng[1,2,*], Satoshi Baba[1,2], Hadar Ben-Gida[1], Philippe Lavoie[1], Stéphane Moreau[2],

[1]Institute for Aerospace Studies, University of Toronto, Toronto, Canada
[2]Mechanical Engineering, Université de Sherbrooke, *patrickgc.deng@mail.utoronto.ca

March 31, 2025

***Abstract*—**This study investigates the dynamics of the wing-tip vortices, focusing on their formation, interaction, and evolution. Using wall-resolved large-eddy simulations (LES), three independent wing-tip vortices on the supercritical wing geometry were visualized, which were coined the primary vortex (PV), secondary vortex (SV), and tertiary vortex (TV). Using the computational tools, the kinematics, dynamics, and surface pressure effects of these vortices are analyzed. The PV, originating from the pressure-side shear layer, exhibits the characteristics of a wake vortex, signified by high velocity strain, a large amplitude wandering, and progressive vorticity dissipation. In contrast, the SV, forming from the suction-side shear layer, retains the property of jet vortex with strong axial momentum and minimal wandering, leading to a more stable and coherent vortex structure. The formation of the TV, driven by the aft pressure side camber, plays a key role in shaping the final helical tip vortex, where momentum transfer and vortex merging define the downstream aerodynamic and acoustic characteristics. The analysis on the invariants of the velocity gradient tensor (QR analysis) highlights fundamental differences in strain-vorticity interactions between the PV and SV, with the PV indicating dominant strain-induced stretching and dissipation, while the SV remains highly vorticity-dominated, sustaining its structure over longer convective timescales.

***Keywords-component*—LES, Tip-Vortex, Vortex Dynamics**

I. Introduction

Wing-tip vortices, generated at the outboard edges of s finite-span wings, are a fundamental aspect of aerodynamic flows and an inevitable flow structures in designing an aerodynamic components such as high-lift devices, helicopter rotors, turbomachines, and axial fans. These vortices exhibit complex three-dimensional structures that evolve while they convect downstream, significantly influencing both aerodynamic performance and aeroacoustic signature. The formation of tip vortices is primarily driven by the tip-pressure difference between the suction and pressure surfaces of an airfoil. This pressure gradient induces a flow from the high-pressure region on the pressure surface to the low-pressure region on the suction surface near the wingtip. Understanding the dynamics of tip vortices is crucial for optimizing aerodynamic efficiency and mitigating noise emissions.

Among the flow features at the wing-tip geometry, the formation of a dual-vortex structure is the most prominent and extensively studied phenomenon both numerically and experimentally for wing tips and flap-side edges [1–5]. This dual-vortex system, consisting of a primary vortex at the tip surface and a secondary vortex on the suction side, is driven by the pressure difference between the pressure and the suction surface, which creates a spanwise cross-flow separation at the corners of the wing tip. Downstream of the wing tip leading edge, a shear layer forms at the pressure surface edge, rolling up into the primary vortex, while the second shear layer at the suction surface edge generates the secondary vortex. These vortices exhibit circumferential flow speed that is comparable in magnitude to the freestream, and grows in size along the streamwise direction. The primary vortex is convected toward the suction surface, eventually merging with the secondary vortex into the tip vortex system [2–4]. Recently, the tri-vortex system was observed on the tip of supercritical profile wings with an additional tertiary vortex, adding to the complexity of flow features present at the tip [6, 7].

Beyond their aerodynamic properties, tip vortices are prominent sources of aeroacoustic emissions, particularly in low-Mach number flows [6]. Their unsteady interactions with the

Sponsors: Bombardier, Natural Sciences and Engineering Council of Canada, the Ontario Research Fund.

airfoil surface generate intense surface pressure fluctuations, inducing density variations in the surrounding fluid that radiate as noise in the far field. The broadband nature of this noise arises from the highly unsteady and multi-scale characteristics of the vortex structures, encompassing contributions from both large-scale coherent motions and small-scale turbulent fluctuations [6].

The overall objective of this research is to apply compressible Wall-Resolved Large-Eddy Simulations (LES) to study the dynamics of the tip-vortex system, specifically investigating the vorticity-strain properties of the tip vortex. The LES was performed on a supercritical finite span wing at a 10° static angle of attack and a Reynolds number of Re = 620,000. This study aims at enhancing the understanding of wing-tip vortex dynamics and their aeroacoustic impacts, contributing to the optimization of aerodynamic designs for improved performance and reduced noise emissions.

II. Methodology

The volume data around the airfoil are obtained from the compressible solver AVBP v7.9, developed by CERFACS [8]. The present configuration utilizes an isolated supercritical wingtip model at an angle of attack of $\alpha = 10^\circ$ with an inlet velocity of $U_\infty = 30$ m/s, corresponding to a chord-based Reynolds number of $Re_c = 620,000$ and a freestream Mach number of $Ma = 0.09$. The velocity gradient tensor $\boldsymbol{A}_{ij} = \nabla \boldsymbol{u} = \partial u_i / \partial x_j$ data was extracted over a 32 ms period from the simulation domain at a sampling frequency of $f_s = 30,000$ Hz was used to calculate the invariants and the rotation and strain tensors. The detailed simulation setup is the same as the one described in the previous work by Deng *et al.* [7].

In particular, $\boldsymbol{A}_{ij}$ characterizes the local fluid kinematics by capturing both the deformation and rotational behavior of a fluid element. It can be decomposed into its symmetric and antisymmetric components as $\boldsymbol{A}_{ij} = \boldsymbol{S}_{ij} + \boldsymbol{\Omega}_{ij}$ where $\boldsymbol{S}_{ij}$ is the *rate-of-strain tensor* and $\boldsymbol{\Omega}_{ij}$ is the *rate-of-rotation tensor*. The rate-of-strain tensor $\boldsymbol{S}_{ij} = \boldsymbol{A} + \boldsymbol{A}^T$ quantifies deformation of the fluid element, representing stretching or compression along principal axes without rigid body rotation. Conversely, the rotation-rate tensor $\boldsymbol{\Omega}_{ij} = \boldsymbol{A} - \boldsymbol{A}^T$ describes the angular velocity of the fluid element, capturing pure rotational motion without any deformation.

The invariants of the velocity gradient tensor provide valuable insight into the local flow structures by characterizing the interplay between strain and vorticity. The characteristic equation of $\boldsymbol{A}$ is:

$$\lambda_i^3 + P\lambda_i^2 + Q\lambda_i + R = 0, \tag{1}$$

resulting in the three principal invariants derived from Equation 1, are the trace P, the second invariant Q, and the third invariant R. These are defined as follows:

$$P = -\nabla \cdot \boldsymbol{u} = -\text{Trace}(\boldsymbol{A}), \tag{2}$$

which is velocity divergence representing local compressibility effects.

$$Q = \frac{1}{2}\left(\|\boldsymbol{\Omega}\|^2 - \|\boldsymbol{S}\|^2\right) = \frac{1}{2}\left(P^2 - \text{Trace}(\boldsymbol{A}^2)\right), \tag{3}$$

which quantifies the competition between rotation and strain, often quoted as the Q–criterion.

$$R = -\det(\boldsymbol{A}) = -\frac{1}{3}\text{Tr}(\boldsymbol{A}^3), \tag{4}$$

which reflects vortex stretching and deformation. Finally, another invariant of the velocity gradient tensor is the discriminant of the characteristic polynomial defined as,

$$\Delta = -\frac{1}{4}P^2Q^2 + Q^3 + P^3R + \frac{27}{4}R^2 - \frac{18}{4}PQR, \tag{5}$$

where Δ, commonly known as the Vieillefosse line, allows for distinguishing between flow regions where vorticity dominates ($\Delta > 0$) versus regions where strain dominates ($\Delta < 0$). The QR space is also scaled according to the local velocity-gradient tensor magnitude with $\text{var}(\boldsymbol{A}) = \overline{\text{Trace}(\boldsymbol{A} - \bar{\boldsymbol{A}})(\boldsymbol{A} - \bar{\boldsymbol{A}})^T}$ following the procedure described by Wu *et al.* [9].

Together, the joint probability density function (PDF) of Q and R with the discriminant can be used to classify local flow structures, and identify regions dominated by vorticity or strain. It provides insight into the underlying dynamics of turbulence by revealing preferred states of strain and rotation, helping to understand vortex stretching, dissipation, and the energy cascade process. From a Lagrangian view, it allows the distinction between four different states of the structure at the location of the fluid particle based on $\Delta = 0$ and $R = 0$:

1) $\Delta < 0, R > 0$, straining structures with flattening,
2) $\Delta < 0, R < 0$, straining structures with elongating,
3) $\Delta > 0, R > 0$, vortical structures with contracting,
4) $\Delta > 0, R < 0$, vortical structures with stretching.

This velocity gradient tensor and its invariants provide insight into the overall dynamics and turbulence characteristics of the flow.

III. Vortex Characteristics

Figure 1 presents the instantaneous isosurface of the Q–criterion with the mean vortex core trajectories color-coded by axial velocity. At the forward region of the tip, the spanwise cross-flow separates at the pressure side-edge, forming a shear layer that rolls up into a large primary vortex (PV) on the tip surface, followed by a secondary vortex (SV) on the suction side due to the side-edge pressure gradient. These vortices grow and expand as they convect downstream with energy fed by their respective shear layers. Near $x/c = 0.7$, a tertiary vortex (TV) forms on the pressure tip after the PV has crossed over to merge with the SV, and at $x/c \approx 0.8$, the PV begins to crossover and impinge on the suction surface, leading to the merging of the PV and SV near $x/c = 0.85$. This interaction facilitates the formation of the TV aft of midchord—a distinctive feature of supercritical profiles [6, 7]. The tertiary vortex further merges with the SV near the trailing-edge, culminating

in a coherent side-edge vortex system beyond the trailing edge, which evolves into the tip vortex as the vortices detach and co-rotate into a helical structure. These shed vortices, driven by shear layer instabilities, play a significant role in both drag and aerodynamic noise production.

To accurately characterize the trajectories of the PV, SV, and TV, a modified predictor-corrector method based on Banks and Singer's approach was employed, involving an initial skeleton approximation by tracing vorticity lines followed by correction based on local maxima of the Q–criterion [10].

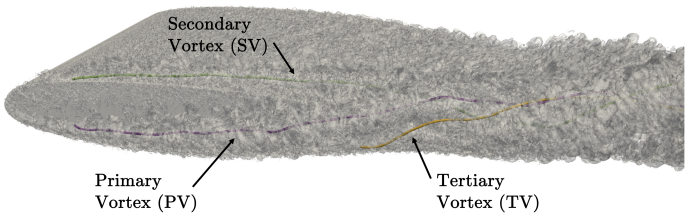

Figure. 1: Instantaneous iso-contour of the Q–criterion ($2 \times 10^5\ s^{-2}$) with mean vortex core trajectories.

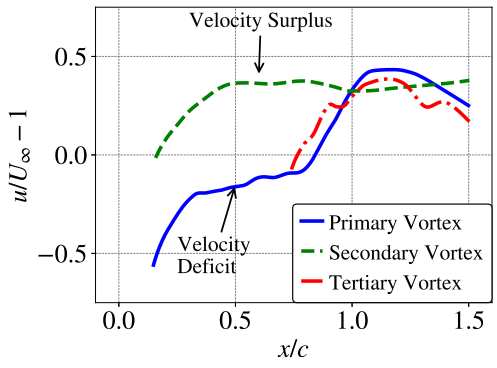

(a)

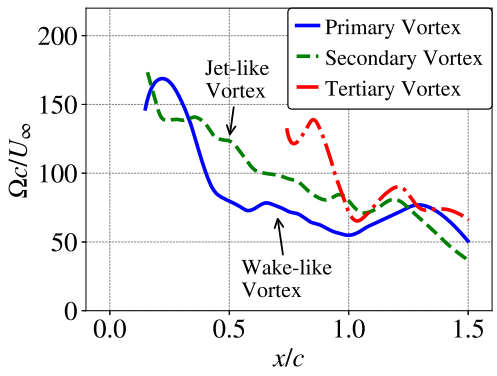

(b)

Figure. 2: Evolution of vortex core velocity and vorticity, a) core velocity deficit, b) core normalized vorticity.

The evolution of the vortex core velocity deficit along the chord is shown in Figure 2a. As the vortices convect downstream, the PV exhibits a notable velocity deficit prior to crossover, consistent with wake-like behavior. This velocity deficit arises due to energy dissipation and the entrainment of low-momentum fluid from the surrounding flow into the vortex core. The deficit is further amplified by the impingement and deformation of the PV, leading to significant loss of vorticity as it expands downstream. In contrast, the SV exhibits a strong velocity surplus at 40 % above the freestream, a hallmark of jet-like vortex behavior. This surplus is a direct consequence of boundary layer acceleration of the SV on the suction surface. This surplus reflects the higher axial momentum retained by the SV, which results from its ability to sustain energy input from its associated shear layer while maintaining a tighter core structure. Following the crossover, the PV core velocity increases due to momentum transfer from the SV during their interaction. The TV forms later in the flow with a velocity deficit similar to the PV, reflecting wake-like characteristics during its early development. The TV forms due to the high aft-camber on the pressure side of the supercritical airfoil, inherits its dynamics from the flow structures left by the PV. The TV develops in a region influenced by the PV decay and crossover. As it progresses downstream, the TV rapidly increases its core velocity during its merger with the SV near the trailing edge, reorganizing its structure and contributing to the formation of a stable tri-vortex system.

The vorticity evolution of the tri-vortex system, illustrated in Fig. 2b, highlights the dynamic redistribution of rotational energy at the wingtip. The PV undergoes substantial vorticity decay due to viscous dissipation and the stretching effects imposed by its impingement on the suction surface. This decay is most pronounced in the downstream regions where the PV interacts and merges with the SV. While the SV also experiences some vorticity decay, it retains a relatively higher rotational strength compared to the PV, enabling it to dominate the flowfield near the trailing edge. This retention is attributed to the SV more coherent core structure and efficient energy input from the suction side shear layer. Collectively, these interactions between the PV, SV, and TV not only shape the final helical tip vortex structure but also play a critical role in aerodynamic noise production, as the redistribution of momentum and vorticity generates broadband sound that radiate into the far field.

IV. Vortex Kinematics

At the tip, the complex flow phenomena associated with the tri-vortex system are inherently unsteady, with each vortex core fostering elliptical instabilities and exhibiting distinct stochastic wandering motions [11]. The instantaneous vortex core positions are analyzed through the three streamwise cut planes shown in Fig. 3. The vortex cores are tracked across 1000 snapshots with a sampling frequency of 33,000 Hz over 3 convective flow-though times. The instantaneous positions of the vortex cores are identified through the local maxima of the Q–criterion, along with their principal axes that illustrate the preferred motion of each vortex.

At $x/c = 0.58$, figure 3a show only the PV and SV, as the TV is yet to develop. The PV exhibits an elliptical

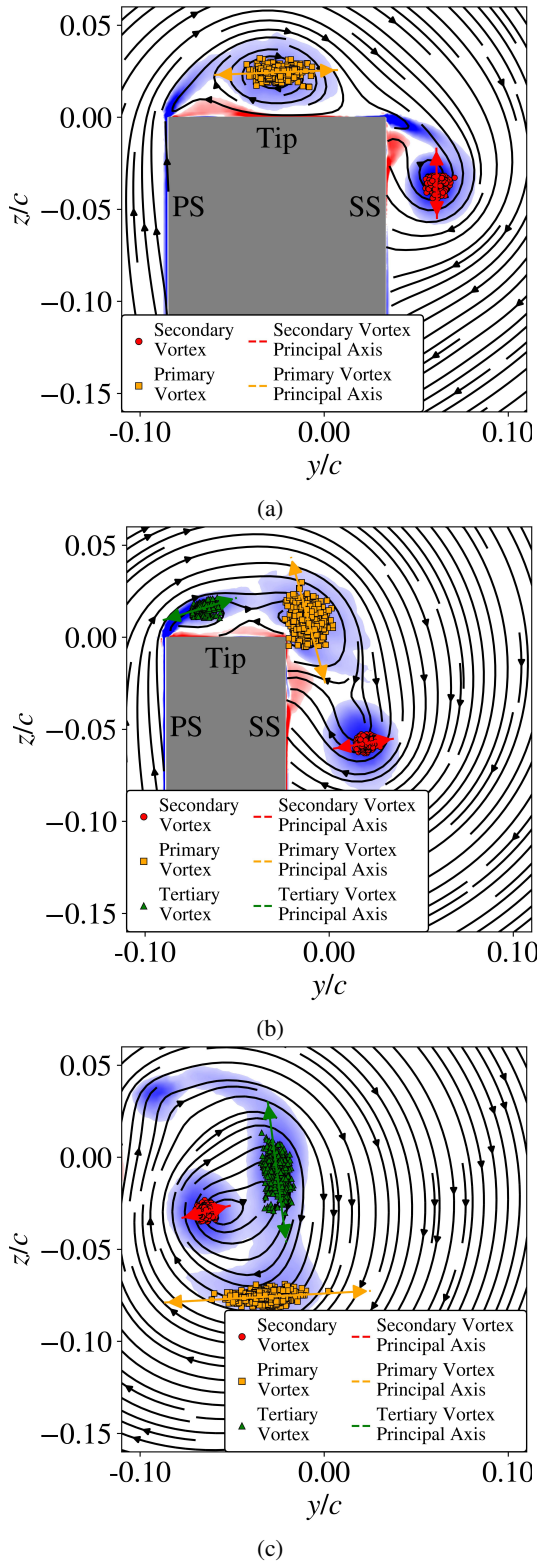

Figure. 3: Instantaneous vortex core position at various streamwise planes with contours of normalized vorticity, a) $x/c = 0.58$, b) $x/c = 0.78$, c) $x/c = 1.05$.

wandering motion with its principal axis oriented parallel to the tip surface. This elliptical wandering profile envelopes the majority of the tip surface leading to vortex scrubbing at the tip surface. In contrast, the SV core maintains a more compact near-circular profile with its principal axis oriented normal to the suction surface, a result of the dominant spanwise crossflow as the SV is pulled inboard. At $x/c = 0.78$, Figure 3b now show all three vortices with varying magnitudes of wandering motion. The PV undergoes crossover as it is being pulled toward the SV. The core maintains its elliptical profile with the principal axis now oriented towards the SV. This PV crossover introduces additional unsteadiness as the PV scrapes the wing-tip corner, the associated vortex deformation and resultant pressure diffraction is then a main noise source at the tip [6]. The SV maintains its compact core structure, but in the absence of energy input from the suction-side shear layer and spanwise momentum transport, its principal axis reorients normal to the wall. Meanwhile, the TV develops from the pressure-side shear layer, following a similar formation mechanism as the PV and initially exhibiting an elliptical profile. Beyond the trailing-edge at $x/c = 1.05$, the tri-vortex system transitions into a helical motion as all three vorticies begin to co-rotate, as seen in Figure 3c. The SV retains its circular profile, indicating a relatively stable structure, while the PV and TV maintain their elliptical profiles, suggesting sustained wandering motion. The large in-plane wandering amplitude and angular momentum of the PV and TV likely drive the helical vortex formation of the combined tip vortex.

A key observation is that the PV exhibits significantly greater instantaneous wandering compared to the SV. This increased wandering is consistent with the wake-like nature of the PV, which is highly susceptible to shear layer instabilities and external flow perturbations. In contrast, the SV, which exhibits jet-like characteristics, follows a more stable trajectory with reduced wandering, likely due to its higher axial momentum and tighter core structure.

V. Vortex Dynamics

The vorticity and strain rate distributions shown in Figures 4a and 4b reveal the underlying mechanisms driving the evolution of the tri-vortex system. The PV, despite receiving higher initial momentum input from the PS shear layer, experiences vorticity decay as it convects downstream as shown in Figure 2b. This decay is primarily attributed to strain-induced dissipation leading to increased wandering of the PV. The strain rate distribution highlights this effect, where the PV interacts with a broad strain regions that deform its core structure and contribute to its instability. Additionally, alternate vortex shedding in the PV suggests a balance between vorticity advection and strain interactions, which further disrupts its coherence and increases its susceptibility to turbulent breakdown.

In contrast, the SV maintains a tighter and more stable core, with lower direct momentum injection after $x/c = 0.58$. However, the SV benefits from boundary layer acceleration on the suction surface, which acts as a stabilizing mechanism by enhancing axial momentum and sustaining coherent rotation.

Unlike the PV, the SV experiences dominant vortex stretching, which allows it to maintain its rotational strength. This is reflected in the strain rate field, where strain effects are comparatively weaker in the SV, leading to a more sustained and localized vortex core. The presence of a high-energy vortex core with limited compression regions indicates that the SV follows a jet-like behavior, where momentum remains concentrated, and strain-induced diffusion is minimal. This fundamental difference in strain-vorticity interactions governs how each vortex evolves within the tri-vortex system.

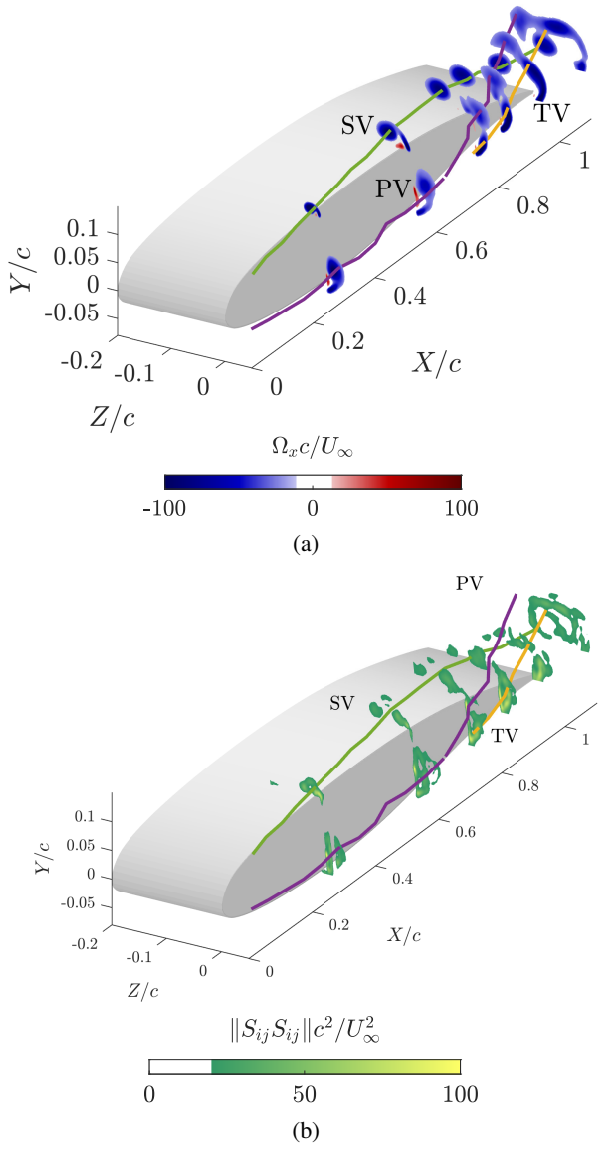

Figure. 4: Mean contours of vorticity and strain-rate at various streamwise locations, a) normalized vorticity, b) normalized strain-rate.

The QR distribution along vortex core are shown by Figure 5a for the PV and in Figure 5b for the SV, starting at $x/c = 0.58$ at $0.08c$ intervals. The PV exhibits a nearly symmetric QR distribution along the core, indicating that rotation and strain effects are balanced throughout its development. This suggests that the PV undergoes continuous strain-vorticity interactions, where rotational strength is progressively weakened by diffusion and vortex deformation. The presence of alternate vortex shedding as seen in Figure 1 further reinforces this observation, as periodic shedding events contribute to fluctuating strain compression and vortex breakup. As the PV convects downstream, its QR distribution shows a broadening of strain-dominated regions, reflecting increasing energy dissipation and a reduction in coherent rotational structures. This is consistent with its wake-like behavior, where rotational energy is gradually lost to turbulence, resulting in increased wandering and instability in the vortex core. Moreover, the presence of the Vieillefosse tail (tear-drop shape) for the PV, where the flow is biased towards Q <0 and R >0 on the discriminant Δ, is a defining feature in most turbulent flows, indicating a dominance of strain and stretching that drives the energy cascade to smaller scales.

In contrast, the SV exhibits a strongly skewed QR distribution towards positive Q–values, which indicates rotation-dominated dynamics with minimal strain-induced dissipation. This skewness highlights the dominance of vortex stretching over strain-induced diffusion, allowing the SV to sustain its rotational strength for a longer distance downstream. The lack of strong strain compression regions suggests that momentum remains concentrated within the core, reducing the likelihood of vortex breakdown. Unlike the PV, the SV rotational coherence is preserved due to the combined effects of suction-side shear layer feeding and boundary layer acceleration, which help stabilize the vortex structure. This is further supported by the absence of the Vieillefosse tail, implying that the SV is less susceptible to turbulent breakdown and energy loss.

The root-mean-square (RMS) surface pressure coefficient ($c_{p,RMS}$) contour shown in Figure 6 highlights the dominant regions of wall-pressure fluctuations near the wingtip, with the primary vortex PV region at the tip being the primary contributor. As previously discussed, the wake-like PV exhibits higher velocity strain and dissipation, leading to momentum diffusion and an unsteady, multi-scale vortex shedding process. This results in a distributed and fluctuating pressure field, characterized by strong localized pressure variations, particularly at the PV impingement and vortex crossover regions. In contrast, the SV creates a significantly smaller pressure footprint, reflecting its higher coherence and jet-like nature, which minimizes unsteady interactions with the surface. The SV sustained axial momentum and reduced wandering contribute to a more localized and stable pressure distribution, limiting its impact on far-field noise compared to the PV. These observations reinforce the role of the PV as the dominant source of aerodynamic noise, where its wake-like behavior and turbulent breakdown amplify wall-pressure fluctuations, making it the primary contributor to far-field noise radiation.

VI. Conclusion

This study provides a detailed investigation into the vortex dynamics of a supercritical arifoil wingtip, focusing on

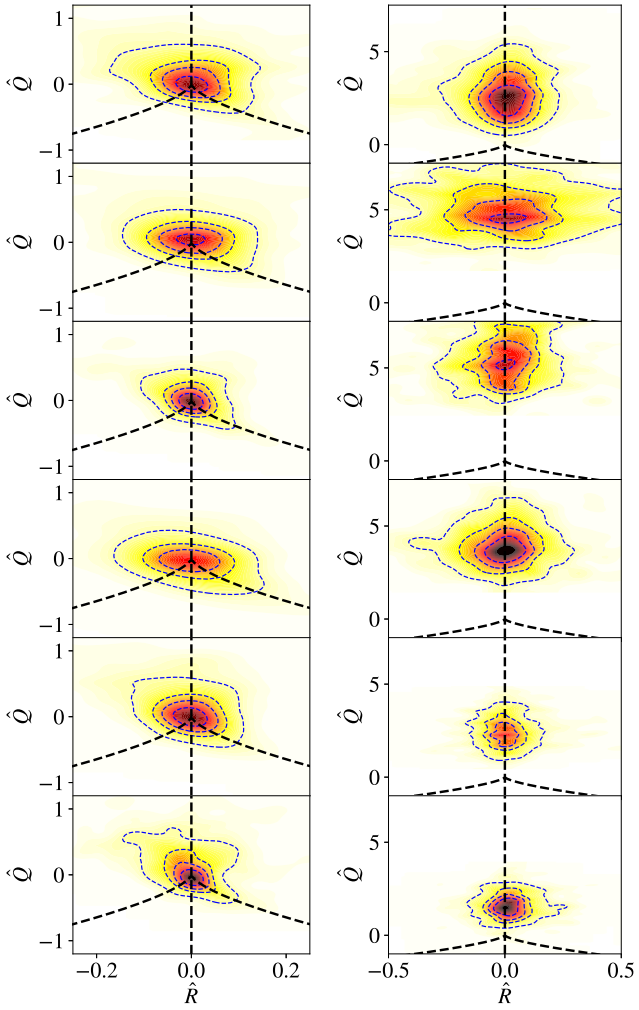

Figure. 5: Probability density function contours of QR development along the mean vortex core, a) PV, b) SV.

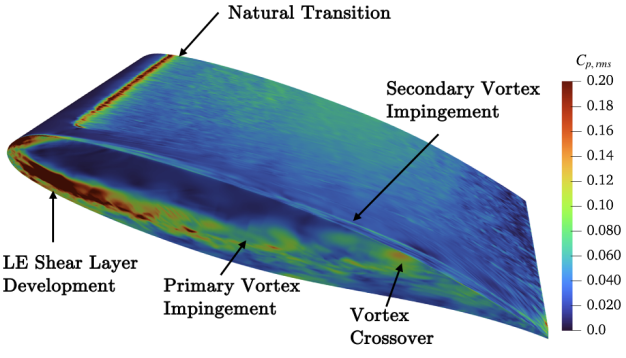

Figure. 6: Contour of the root mean square of the pressure coefficient.

the formation, interaction, and downstream evolution of the primary, secondary, and tertiary vorticies. The analysis reveals that the PV, originating from the pressure-side shear layer, exhibits wake-like characteristics with high velocity strain, significant wandering, and progressive turbulent dissipation, making it the primary source of surface pressure fluctuations and subsequently far-field noise. In contrast, the SV, sustained by suction-side boundary layer acceleration, retains jet-like properties, with strong axial momentum and minimal wandering, leading to a more coherent and stable vortex structure. The formation of the TV, initiated by the PV-SV interaction, plays a crucial role in shaping the final helical tip vortex, with the merging process facilitating the redistribution of momentum and rotational energy. The QR analysis highlights the dominant strain-induced dissipation in the PV, driving its breakdown and increasing wall-pressure variations, while the SV remains rotation-dominated, resisting turbulent dissipation. The resulting tri-vortex system governs the aerodynamic performance and acoustic footprint of the wingtip, with implications for vortex control strategies, noise mitigation, and aerodynamic efficiency.

References

[1] S. A. Mclnerny, W. C. Meecham, and P. T. Sodermant, "Pressure fluctuations in the tip region of a blunt-tipped airfoil," *AIAA Journal*, vol. 28, no. 1, pp. 6–13, 1989.

[2] M. R. Khorrami and B. A. Singer, "Stability analysis for noise-source modeling of a part-span flap," *AIAA Journal*, vol. 37, pp. 1206–1212, October 1999.

[3] W. J. Devenport, M. C. Rife, S. I. Liapis, and G. J. Follin, "The structure and development of a wing-tip vortex," *Journal of Fluid Mechanics*, vol. 312, pp. 67–106, 2006.

[4] T. Imamura, S. Enomoto, and K. Yamamoto, "Noise simulation around NACA0012 wingtip using Large Eddy Simulation," *Transactions of the Japan Society for Aeronautical and Space Sciences*, vol. 55, no. 4, pp. 214–221, 2012.

[5] R. Vinuesa, P. S. Negi, M. Atzori, A. Hanifi, D. S. Henningson, and P. Schlatter, "Turbulent boundary layers around wing sections up to rec= 1,000,000," *International Journal of Heat and Fluid Flow*, vol. 72, pp. 86–99, 2018.

[6] S. Baba, H. Ben-Gida, G. C. Deng, O. Stalnov, S. Moreau, and P. Lavoie, "Experimental aeroacoustic characterization of a supercritical wing-tip model," in *2024 AIAA/CEAS Aeroacoustics Conference*, pp. AIAA–2024–3124, 2024.

[7] G. C. Deng, S. Baba, S. Moreau, and P. Lavoie, "Large-eddy simulation and aeroacoustic prediction of supercritical airfoil side-edge noise," *AIAA Journal*, vol. 62, no. 9, pp. 3340–3353, 2024.

[8] T. Schonfeld and M. Rudgyard, "Steady and unsteady flow simulations using the hybrid flow solver avbp," *AIAA Journal*, vol. 37, no. 11, pp. 1378–1385, 1999.

[9] H. Wu, S. Moreau, and R. Sandberg, "Effects of pressure gradient on the evolution of velocity-gradient tensor invariant dynamics on a controlled-diffusion aerofoil at $Re_c = 150000$," *Journal of Fluid Mechanics*, vol. 868, pp. 584–610, 2019.

[10] D. C. Banks and B. A. Singer, "A predictor-corrector technique for visualizing unsteady flow," *IEEE Transactions on Visualization and Computer Graphics*, vol. 1, no. 2, pp. 151–163, 1995.

[11] H. Ben-Gida, S. Baba, O. Stalnov, S. Moreau, and P. Lavoie, "Experimental characterization of the side-edge triple-vortex system on a supercritical wing model," in *2024 AIAA/CEAS Aeroacoustics Conference*, pp. AIAA–2024–3173, 2024.